WPMST1-CPR(18) 18829

E Thorn et al.

MEMOS 3D modelling of ELM-induced transient melt damage on an inclined tungsten surface in the ASDEX Upgrade outer divertor

Preprint of Paper to be submitted for publication in Proceeding of 23rd International Conference on Plasma Surface Interactions in Controlled Fusion Devices (PSI-23)

This work has been carried out within the framework of the EUROfusion Consortium and has received funding from the Euratom research and training programme 2014-2018 under grant agreement No 633053. The views and opinions expressed herein do not necessarily reflect those of the European Commission.

MEMOS 3D modelling of ELM-induced transient melt damage on an inclined tungsten surface in the ASDEX Upgrade outer divertor

E. Thorén[a], S. Ratynskaia[a], P. Tolias[a], R. A. Pitts[b], K. Krieger[c], M. Komm[d], M. Balden[c], the ASDEX-Upgrade Team[c], and the EUROfusion MST1 Team*

[a] *Space and Plasma Physics - KTH Royal Institute of Technology, SE-10044 Stockholm, Sweden*
[b] *ITER Organization, Route de Vinon-sur-Verdon, CS 90 046, F-13067, St. Paul Lez Durance, France*
[c] *Max-Planck-Institut fr Plasmaphysik, 85748, Garching b. Mnchen, Germany*
[d] *Institute of Plasma Physics CAS, Za Slovankou 3, 182 00 Prague 8, Czech Republic*

Abstract

The first MEMOS 3D simulations of liquid metal motion on an inclined bulk tungsten sample transiently molten by edge-localized modes (ELMs) are reported. The exposures took place at the outer ASDEX-Upgrade divertor with the tungsten surface tangent intersecting the magnetic field at $\sim 18°$. Simulations confirm that the observed poloidal melt motion is caused by the volumetric $\boldsymbol{J} \times \boldsymbol{B}$ force with $\boldsymbol{J}$ the bulk replacement current triggered by thermionic emission. The final erosion profile and total melt build up are reproduced by employing the escaping thermionic current dependence on the incident heat flux derived from dedicated particle-in-cell simulations. Modelling reveals that melt dynamics is governed by the volumetric Lorentz force, thermo-capillary flows due to thermal surface tension gradients and viscous deceleration. The effect of the evolving surface deformation, that locally alters the field-line inclination modifying the absorbed power flux and the escaping thermionic current, in the final surface morphology is demonstrated to be significant.

1. Introduction

ITER will begin operation with a full tungsten (W) divertor, which introduces the risk of deep recrystallization and surface or even bulk melting. The design choices of the W divertor monoblocks have to ensure their lasting power handling capability well into the nuclear phase [1, 2]. To this end, one of the primary concerns refers to the occurrence and prevalence of monoblock melting during ELMing H-mode operation. Molten metals, that are formed in the extreme strongly magnetized divertor environment, will be subject to various plasma-induced forces some of which are capable of generating macroscopic material flow. Melt displacements will be ultimately arrested by resolidification and result in enhanced surface erosion of the monoblocks, thus compromising their power handling capabilities.

A cross-machine experimental study has been recently initiated [2] aiming to improve physics understanding of transient W melt dynamics in the divertor environment. Several melting experiments have reported that liquid W was mainly displaced along the poloidal direction [3, 4, 5, 6, 7]. Such a material displacement is consistent with a dominant volumetric $\boldsymbol{J} \times \boldsymbol{B}$ force density acting on the molten layer, where $\boldsymbol{B}$ is the toroidal magnetic field and $\boldsymbol{J}$ is the replacement current density flowing through the liquid layer to compensate for surface charge loss due to electron emission [2]. In the experimentally accessible parameter space, owing to the high W melting point, electron emission can be mainly attributed to thermionic emission.

MEMOS (Melt Motion at Surfaces) is a simulation tool that numerically solves the heat conduction equation coupled with the incompressible Navier-Stokes equations in the shallow water approximation [8, 9]. MEMOS 3D has been employed to model recent melt experiments in JET and ASDEX-Upgrade (AUG) [4, 5, 10]. The JET exposures featured a W leading edge intercepting nearly the full field-line parallel plasma heat flux, a sample geometry which was later also employed in the AUG experiments.

The AUG experiments also utilized a *sloped* sample [5], where the exposed surface intersects the magnetic field at $\sim 18°$. Such a low inclination angle results in the reduction of the absorbed power flux and the suppression of the escaping thermionic current, with both effects inhibiting surface erosion [2, 11]. However, the sloped sample exposures were more extended compared to the leading edge, so that the threshold to sustained melting was reached yielding a significant overall melt displacement. In addition, variations of the local normal due to melt motion induced surface deformation significantly alter the projected area at such field-line inclination (in contrast to the leading edge geometry). In this work, the first simulations of the AUG sloped surface melting experiments are reported. Numerical and modelling modifications which were required in order to address the aforementioned characteristics of the inclined exposure geometry are discussed in details. The simulated final erosion profiles and the total melt build-up are compared with the observations.

*See author list of Ref.[21].

2. Experimental input

The technical details of the recent transient W melting experiments carried out in ASDEX-Upgrade have been thoroughly described in Ref.[5]. All ELMing H-mode discharges were similar: $B_\mathrm{t} = -2.5\,\mathrm{T}$, $I_\mathrm{p} = 0.8\,\mathrm{MA}$ and $P = 7.5\,\mathrm{MW(NBI)}$, $2\,\mathrm{MW(ECRH)}$. The sloped exposures concerned four discharges with a steady outer strike point and a gradually increasing duration $(0.5, 1, 1.5, 2\,\mathrm{s})$. The experiments were designed in a manner that avoided sustained melting of the W sample. Here, we report simulation results for the last and longest exposure, shot #33511.

The only experimental input for the simulations is the field-line parallel heat flux. Since no direct IR measurements of the exposed sample were available, the heat flux was evaluated from IR observations of a toroidally displaced flat sample, justified by toroidal symmetry. Within the optical approximation (in which plasma particles are assumed to follow the magnetic field lines and the effects of gyro-motion or sheath electrostatic fields on particle trajectories are ignored), the value of the field-line parallel heat flux at the position of the sloped sample can be deduced. The ELM peaks reach $q_{||} \sim 1\,\mathrm{GW/m^2}$, and the ELM frequency is $\sim 70\,\mathrm{Hz}$. Details of the spatio-temporal profile of power flux employed here can be found in Ref.[10].

The flat geometry of the tile and sample mounting inaccuracies can introduce systematic errors in the deduced heat flux magnitude of about 20%. Moreover, the sampling time of the IR observations (330 μs) is on the order of the ELM rise time, which may also lead to underestimation of the heat flux by $\sim$ 20%.

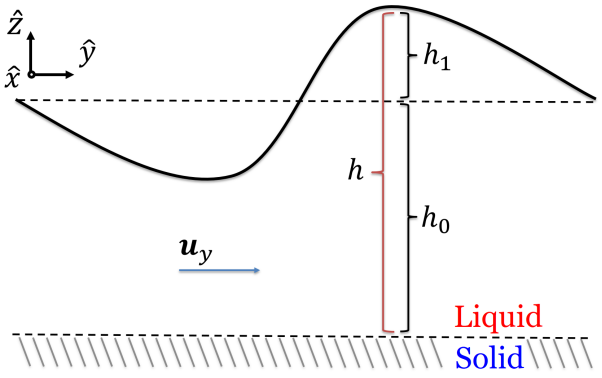

Figure 1: A sketch of the system defining the melt depth $h = h_0 + h_1$, where h_0 is the position of the liquid-solid interface, and h_1 is the position of the perturbed surface, both with respect to the initial pristine surface. Note that h_1 and h_0 can have both positive and negative values. $V_\mathrm{m} = \partial h_0/\partial t$ is the surface normal interface velocity of the melting front, negative when resolidication takes place and positive when melting occurs. One of the depth averaged tangential fluid velocity component is indicated, $u_y(x,y) = \frac{1}{h}\int v_y(x,y,z)dz$. The MEMOS 3D local coordinate system (cartesian) is also displayed.

3. Updates and problem implementation

3.1. The MEMOS 3D code

MEMOS 3D couples the heat diffusion equation in the solid and liquid metal with the incompressible Navier-Stokes equations for the liquid phase [8]. The latter are averaged across the melt layer depth, resulting in the shallow water equations [12]. This reduces the dimensionality of fluid motion by one, restricting the unknown velocities to be tangential to the boundaries of the heat conduction domain. The resulting equations are

$$\frac{\partial h}{\partial t} + \frac{\partial (h u_i)}{\partial x_i} + \frac{\partial (h u_j)}{\partial x_j} = V_\mathrm{m}\,, \tag{1}$$

$$\rho_\mathrm{m}\left[\frac{\partial u_i}{\partial t} + u_j\frac{\partial u_i}{\partial x_j} + u_i\frac{\partial u_i}{\partial x_i}\right] = -\frac{\partial p}{\partial x_i} + (\boldsymbol{J}\times\boldsymbol{B})_i + \mu\frac{\partial^2 u_i}{\partial x_i^2} + \frac{3}{2h}\frac{\partial \sigma}{\partial T}\frac{\partial T_s}{\partial x_i} - 3\mu\frac{u_i}{h^2}\,, \tag{2}$$

$$\rho_\mathrm{m}\left[\frac{\partial u_j}{\partial t} + u_i\frac{\partial u_j}{\partial x_i} + u_j\frac{\partial u_j}{\partial x_j}\right] = -\frac{\partial p}{\partial x_j} + (\boldsymbol{J}\times\boldsymbol{B})_j + \mu\frac{\partial^2 u_j}{\partial x_j^2} + \frac{3}{2h}\frac{\partial \sigma}{\partial T}\frac{\partial T_s}{\partial x_j} - 3\mu\frac{u_j}{h^2}\,, \tag{3}$$

$$\rho_\mathrm{m} c_\mathrm{p}\frac{\partial T}{\partial t} = \nabla\cdot(k\nabla T) + \rho_\mathrm{e}|\mathbf{J}|^2 - T\frac{\partial S}{\partial T}\mathbf{J}\cdot\nabla T \tag{4}$$

where u_i and u_j are the depth averaged tangential fluid velocity components (cartesian coordinates are employed) and V_m is the surface normal interface velocity of the melting front, defined as the time derivative of the melt depth determined by the heat transfer module. The other field quantities $(\mathbf{J}, \mathbf{B}, p, h, T_\mathrm{s}, T)$ denote the replacement current density, magnetic field, pressure, melt layer height (or depth), surface temperature and bulk temperature, respectively. A sketch of the system introducing main characteristics of the melt motion is presented in Fig.1. The material properties $(\sigma, \mu, \rho_\mathrm{m}, c_\mathrm{p}, k, S, \rho_\mathrm{e})$ are the surface tension, dynamic viscosity, mass density, specific heat capacity, thermal conductivity, absolute thermoelectric power and electrical resistivity, whose temperature dependence is taken into account according to a recent literature survey [13]. The notation $(\boldsymbol{J}\times\boldsymbol{B})_{i,j}$ is employed for the depth averaged tangential components of the Lorentz force density.

Concerning the heat diffusion, incoming plasma flux constitutes a boundary condition for Eq.(4), and is determined experimentally (see Sec.2). Note that for the moderate, $< 1\,\mathrm{m/s}$, melt velocities encountered in the present simulations, the surface-normal temperature diffusion across the melt layer is much larger than the convective temperature transport in the surface-tangential direction, thus only the partial temporal derivative of the temperature has been retained in Eq.(4). In addition, for the bulk current density values relevant for the present simulations, Ohmic heating is negligible with respect to the incident plasma heat flux (deposited across a characteristic heat diffusion length). Finally, estimates of the

magnitude of Thomson heating, the last term of Eq.(4), employing values of $\partial S/\partial T$ for solid W [14, 15] in absence of liquid phase measurements, have also revealed a negligible contribution to volumetric heating.

3.2. Numerical and modelling updates

Some unique characteristics of the sloped exposure geometry, in particular the relatively large melt displacement as well as the impact of surface deformation on the absorbed power flux and the escaping thermionic emission current, necessitated some modifications in the structure of the code and some updates in the incorporated physical models, which are outlined in what follows.

Heat conduction domain. Initially, this domain is constructed in a manner that closely follows the 3D geometry of the exposed sample. Naturally, the time evolving boundary of the sample encloses the fluid domain. Since the hydrodynamic motion deforms the sample's boundary, the heat conduction domain should also evolve. Therefore, in a rigorous treatment, it is necessary to continuously re-evaluate the 3D domain. Previous simulation works with MEMOS 3D have circumvented this complication invoking two assumptions; *(1) The melt displacement in each melt event (ELM) is small compared to the melt depth.* Within this assumption, the mass continuity equation, Eq.(1), can be rewritten as $\partial h_1/\partial t + \partial(h_0 u_i)/\partial x_i + \partial(h_0 u_j)/\partial x_j = 0$ by employing $h = h_0 + h_1 \approx h_0$ and $\partial h_0/\partial t = V_{\rm m}$. Here h_0 is the position of the liquid-solid interface, and h_1 is the position of the perturbed surface, both with respect to the initial pristine surface, see Fig.1. *(2) The change in the surface temperature response as a consequence of accumulated surface deformation is small.* This is fulfilled when the local radius of curvature of the deformed surface, $R_{\rm def}$, is much larger than the typical heat diffusion length for the duration of a melt event (the latter can be approximated by the thickness of the melt layer). These simplifications remove the two-way coupling between fluid motion and heat conduction, *i.e.* the fluid motion relies on input from heat conduction, but not vice versa. In the exposure simulated here, only assumption (*2*) is valid, with $h_0/R_{\rm def} < 0.1$. Due to significant melt displacement at the sustained melting threshold ($h_1 \sim h_0$), assumption (*1*) is violated. Thus, mesh restructuring techniques from MEMOS 2D have been extended to MEMOS 3D and are employed in the simulations presented herein.

Absorbed power flux. The plasma heat flux incident on the heat conduction boundary is calculated from the given field-line parallel heat flux $q_{||}$ within the optical approximation. The angle between the toroidal magnetic field and the pristine surface tangent is $\alpha_0 = 17.8°$, resulting in the absorbed power flux $q_\perp = q_{||}\sin(\alpha_0)$. Melt motion will lead to surface deformation, thus the surface tangent will be spatially varying, subsequently altering the projected area in the optical approximation. As a result of the oblique magnetic field incidence, the effective change in the projected area can be significant. In order to account for this effect, the absorbed power flux $q_\perp(\alpha)$ is calculated by the expression

$$q_\perp(\alpha) = \begin{cases} F_{\rm OA}\, q_{||}\sin(\alpha) + (1-F_{\rm OA})\, q_{||}\sin(\alpha_0) & \alpha \le \pi \\ (1-F_{\rm OA}) q_{||}\sin(\alpha_0) & \alpha > \pi\,, \end{cases} \tag{5}$$

where $0 \le F_{\rm OA} \le 1$ denotes the fraction of the heat flux which is purely optical. For non-shadowed regions, the heat flux is decomposed to a directional inclination-dependent contribution and a uniform smoothed-out contribution. For shadowed regions, only the second contribution makes sense. The optical heat loading is recovered in the limit $F_{\rm OA} = 1$, whereas a uniform heat loading emerges when $F_{\rm OA} = 0$.

Replacement current. A rigorous approach was recently formulated for the replacement current triggered by thermionic emission (TE) which is based on the magnetostatic limit of the resistive thermoelectric magnetohydrodynamic description of the liquid metal [18]. The approach results in a well-defined boundary value problem concerning the whole conductor (where TE serves as the only non-trivial boundary condition) for whose numerical solution a dedicated MEMOS module was developed. This enabled the thorough investigation of the general characteristics of the replacement current for both sloped and leading edge exposures [18]. In the former case, the sample geometry is such that depth-variations of the replacement current inside the melt layer are negligible. As a consequence, the boundary value problem can be circumvented and the bulk replacement current can be set equal to the surface TE current density for each surface element.

Thermionic current. As evident from the discussion above, an accurate description of the TE current density is crucial for a quantitative comparison with the experiment, since it essentially determines the $\mathbf{J}\times\mathbf{B}$ force density driving melt motion. The geometry of interest requires a self-consistent treatment of the entangled effects of space-charge limitation and prompt Larmor re-deposition on the escaping TE current [11]. For this reason, dedicated particle-in-cell (PIC) simulations were carried out with the 2D3V SPICE2 code for the present inter and intra-ELM AUG parameters [16]. The PIC simulations assumed a collisionless plasma with a prescribed sheath edge and a homogeneous surface temperature of the material boundary [11, 16]. The strong impact of magnetic field inclination on the limited value of the escaping current was revealed; more than an order of magnitude reduction for $\alpha = 18°$ (sloped) compared to $\alpha = 90°$ (leading edge). The results also revealed that the limited TE current exhibits a Child-Langmuir type scaling with the plasma parameters. With a few reasonable additional assumptions for the ELMy plasma and the sheath heat transmission, this scaling can be translated into a dependence on the incident field-line parallel heat flux $q_{||}$ [10]. Overall, the escaping TE current density employed in MEMOS is described by the Richardson-Dushman formula up to a minimum $q_{||}-$dependent surface temperature $T^{\rm lim}(q_{||})$ beyond

which it remains constant having entered the space-charge limited regime. For the sloped exposure of the pristine surface $\alpha = 18°$, we have

$$\mathrm{J_{th}}(T_\mathrm{s}, q_{||}) = \begin{cases} A_\mathrm{eff} T_\mathrm{s}^2 \exp\left(-\dfrac{W_\mathrm{f}}{k_\mathrm{b} T_\mathrm{s}}\right) & T_\mathrm{s} \leq T^\mathrm{lim}(q_{||}) \\ 1.38 \times 10^3 \, q_{||}^{1/3} & T_\mathrm{s} \geq T^\mathrm{lim}(q_{||}) \end{cases} \tag{6}$$

where k_b denotes the Boltzmann constant, $W_\mathrm{f} = 4.55\,\mathrm{eV}$ and $A_\mathrm{eff} = 60\,\mathrm{A\,cm^{-2}K^{-2}}$ for polycrystalline W.

As aforementioned, in the scenarios of interest, the local inclination angle will be spatially varying owing to the surface deformation. Complementary PIC simulations were recently carried out for a wide range of magnetic field inclination angles aiming to generalize Eq.(6) for arbitrary inclinations [17]. The simulations once again revealed the emergence of a limited TE current density that scales with the plasma background as well as the inclination angle. For an arbitrary $\alpha \leq \pi$, we have

$$\mathrm{J_{th}}(T_\mathrm{s}, q_{||}, \alpha) = \begin{cases} A_\mathrm{eff} T_\mathrm{s}^2 \exp\left(-\dfrac{W_\mathrm{f}}{k_\mathrm{b} T_\mathrm{s}}\right) & T_\mathrm{s} \leq T^\mathrm{lim}(q_{||}, \alpha) \\ 1.48 \times 10^4 \sin^2(\alpha) \, q_{||}^{1/3} & T_\mathrm{s} \geq T^\mathrm{lim}(q_{||}, \alpha) \end{cases} \tag{7}$$

which nearly collapses to Eq.(6) for $\alpha = 18°$.

3.3. Simulation scenarios

Two assumptions were followed for the thermionic current specification and the heat flux loading of the sample. In the *pristine surface* simulations, the effect of the spatial variations of the surface normal on the escaping current and the absorbed power was neglected. Therefore, the thermionic current was described by Eq.(6) and the absorbed heat flux by Eq.(5) with $F_\mathrm{OA} = 0$. On the contrary, in the *corrugated surface* simulations, the generation of shadowed areas was taken into account, where an upstream peak occludes the plasma and the corresponding field line intersects the surface twice. In these areas, the detailed physics of the sheath heat transmission and electron emission are very involved [19], thus a simplified treatment was pursued. The thermionic current was described by Eq.(7) for $0 \leq \alpha \leq \pi$ and considered zero when $\pi \leq \alpha \leq 2\pi$. The absorbed heat flux was described by Eq.(5) with $F_\mathrm{OA} = 2/7$, which is equal to the electron fraction of the ambipolar heat flux. The remaining 5/7 fraction, which corresponds to the ion contribution, has been distributed uniformly in both the optical and shadowed regions. This is a reasonable assumption given that the ion gyro-radius ($\sim 0.4 - 0.8\,\mathrm{mm}$) is of the order of the typical corrugation height [20].

4. Results and discussion

4.1. Temperature response

MEMOS 3D simulations with the heat conduction module revealed that, for the pristine W surface, transient melting cannot be achieved with the specified heat flux. Due to the lack of direct IR observations of the sloped sample, there can be no real-time comparison between the simulated and the experimental surface temperatures. In the light of such uncertainties in the surface temperature, the heat flux has been uniformly increased at all times by multiplying with a constant pre-factor and the simulation output has been probed for various values of this pre-factor.

The maximum temperature attained in the pristine W surface has been plotted in figure 2 as a function of time, for the pre-factors 1 (un-altered flux), 1.2 and 1.25. The ELM temperature excursions are $\Delta T_\mathrm{s} \sim 400 - 500\,\mathrm{K}$. This implies that for transient W melting to take place, the base (inter-ELM) surface temperature has to exceed 3200 K, which only occurs in the last $\sim 0.5\,\mathrm{s}$ of the exposure. Transient melting is achieved for the pre-factor 1.2, whereas the base temperature reaches the threshold for sustained melting for the pre-factor 1.25. Following the evolution of the base surface temperature, it is apparent that the time window for pure transient melting is quite short ($\leq 0.5\,\mathrm{s}$). It is evident that, due to the proximity to sustained melting, the melt motion output is very sensitive to the precise value of this ad-hoc pre-factor. The employed values of the pre-factor are within uncertainties of the experimental heat flux discussed in Sec.2.

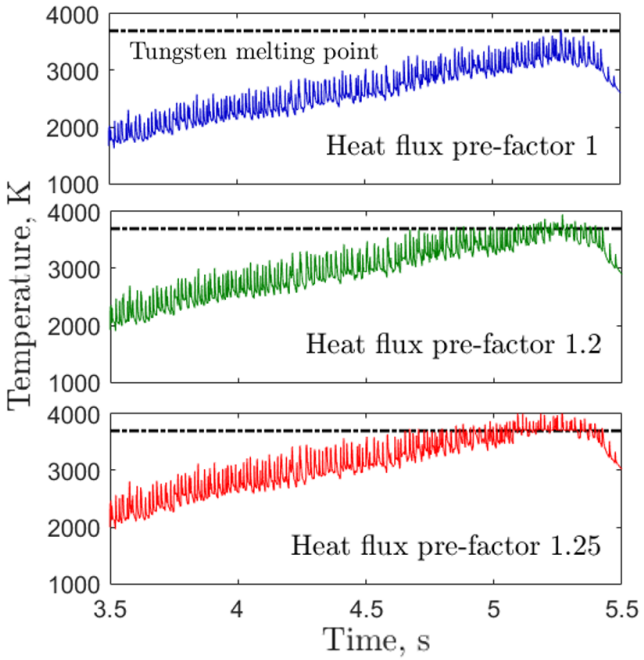

Figure 2: The maximum temperature attained in the pristine surface as a function of time (the last 2 s of the exposure are plotted) for three gradually increasing heat flux pre-factors. The dashed line indicates the W melting point $T_\mathrm{m} = 3695\,\mathrm{K}$.

4.2. Melt motion and macroscopic surface erosion

The simulated melt motion and surface deformation are compared with results of post-mortem surface analysis,

since no real-time observations of the sloped sample were available. In figure 3(a), the post-exposure height map of the sample is shown as measured by laser profilometry [5]. Height deformation reaches a maximum of 600 μm and a displaced material volume of 4 mm^3 has been measured [5]. Melt motion is observed mainly along the poloidal direction (downwards on the page), consistent with the $\mathbf{J} \times \mathbf{B}$ direction. The simulated surface profiles have been plotted alongside the experimental height map.

In the *pristine surface simulations*, local surface normal variations are ignored in the thermionic emission and heat loading. For a 1.25 pre-factor, the total melt displacement is 4.1 mm^3, matching the experimental value. The melt velocity peaks at 0.4 m/s and the maximum melting duration is 15 ms. For higher values of the pre-factor, there is a transition into sustained melting and melt displacement becomes severe. This contradicts the observations, verifying that sustained melting could not have taken place in the experiment. In figure 3(b), the ridges are formed by accumulated melt events. As the liquid layer is accelerated, material builds up at the lower edge of the molten patch before re-solidifying as a ridge. Since the ELM strike position and deposited energy are quite irregular [10], several adjacent ridges are generated. Depending on the position of each transient melt pool, existing ridges may either remelt and be displaced or build up further. The cumulative result consists of a few pronounced ridges on the surface, providing an explanation for the morphology of figure 3(a).

In the *corrugated surface simulations*, local surface normal variations and shadowed areas are considered in the thermionic emission and heat flux loading. Figure 3(c) displays the final erosion profile, which reveals that W melt motion is more pronounced on the right hand side of the exposed surface and that material build-up tends to accumulate into a thin angled stripe at the bottom right side of the eroded spot. These results can be understood by considering the crater formed at the poloidal position ~ 30 mm. The magnetic field lines impinge from the left, which means that the right hand side of the crater leans more sharply into the field-lines than the left side and more power flux is absorbed. Moreover, a larger current density escapes from the right side due to the steep field line inclinations, see figure 3(e), as compared to the pristine surface simulations, see figure 3(d). Both effects, increased heat flux absorption and larger escaping TE current, enhance melt motion. As the sample surface continues to erode, the region of larger heat absorption continuously shifts to the right side. Notice also that in figure 3(d), extended regions of the surface emit a similar current density, because the space-charge limited regime is reached for temperatures well below the melting point for the pristine surface [16].

The adjustment of the heat flux pre-factor in order to reach transient melting, implemented in a simplified though transparent manner (a constant factor in front of $q_\perp(\mathbf{r}, t)$), may result in an unfaithful representation of the finer details of the flux, given the sources of uncertainties discussed in the Sec.2. With the chosen pre-factor, values for the height of the erosion profile and displaced melt volume match the observations reasonably well. The main qualitative picture of the ridge formations and right-left asymmetry is also replicated in the simulations. Some dissimilarities in the erosion profile pattern do exist but in light of the inaccuracies of the heat flux input, the overall agreement can be judged satisfactory.

4.3. Melt acceleration

Overall, the simulations yielded an adequate agreement with the experiment. This suggests that the three sources of fluid acceleration which are incorporated in the Navier-Stokes equations, see Eqs.(2,3), suffice to capture the main aspects of melt dynamics. Their role is discussed below.

Volumetric Lorentz force. The $\boldsymbol{J} \times \boldsymbol{B}$ force is responsible for the bulk poloidal acceleration of the melt layer. For $\alpha = \alpha_0 = 17.8°$, the maximum emitted current density during an ELM is $\sim 1\,\mathrm{MA/m^2}$, resulting in an instantaneous maximum acceleration of $\sim 150\,\mathrm{m/s^2}$. For larger inclination angles, the emitted current reaches higher values, see figure 3(e), and so does the melt acceleration.

Thermo-capillary flow. The large surface temperature gradients result in appreciable surface tension gradients leading to the exertion of an interfacial force. Since surface tension decreases for higher temperatures [13], the liquid is pulled away from the hot areas towards the surrounding colder areas. This force is the only source of toroidal acceleration, in absence of a toroidal component of the $\boldsymbol{J} \times \boldsymbol{B}$ force. Generally, this effect does not result in bulk melt displacement, since its magnitude is significantly smaller than the dominant $\boldsymbol{J} \times \boldsymbol{B}$ force.

Viscous forces in the laminar assumption. From the no-slip condition realized at the solid boundary (bottom of the melt pool), a velocity gradient arises through the melt. An average decelerating stress on the melt layer can be deduced by assuming a laminar shear flow and a parabolic dependence of the fluid velocity on the melt depth [12]. For the highest ~ 0.5 m/s velocities, this deceleration can be comparable to the $\boldsymbol{J} \times \boldsymbol{B}$ acceleration.

5. Summary and conclusions

MEMOS 3D has been employed for the first time for the simulation of macroscopic motion in a transiently molten *inclined* W surface. The sample was exposed in the ASDEX Upgrade outer divertor during ELMing H-mode discharges. The implementation of the problem necessitated code modifications (re-evaluation of heat conduction domain at each time step to account for surface deformation) and modelling updates (thermionic emission, heat flux loading accounting for surface normal variations).

The simulations revealed that the incident heat flux, which constitutes the only experimental input, must be increased for transient W melting to be achieved. As a result of the moderate surface temperature excursions during ELMs, the time window between purely transient and

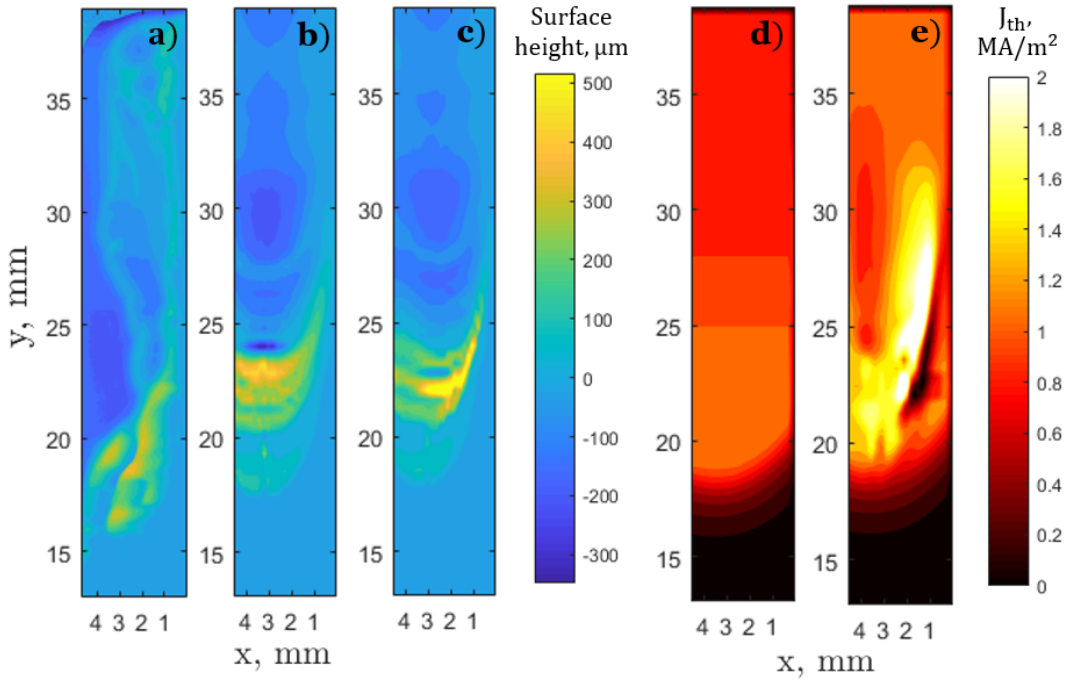

Figure 3: (a) Post-mortem measurements of the exposed surface [5]. (b,c) Simulated final surface morphology profiles for the pristine and corrugated surface. (d,e) Snapshots of the escaping current density typical for the pristine and corrugated surface. Here $\hat{x}$ and $\hat{y}$ are oriented roughly along toroidal and poloidal directions, respectively.

sustained melting is quite short, ~ 0.5 s. Optimal results for melt displacement are recovered close to the threshold of sustained melting, with a 1.25 constant heat flux prefactor. Sustained W melting could not have been realized since it would lead to severe melt displacement contradicting the experimental observations.

The simulated surface deformation at the end of the exposure has been compared to the post-mortem height-map of the exposed sample. The experimental melt displacement volume is well reproduced as well as the deformation structure, with most of the displacement along the poloidal direction due to the dominant $\boldsymbol{J} \times \boldsymbol{B}$ force. The observed ridges in the exposed surface are attributed to the liquid build-up at the edge of the melt pool during individual melt events.

Surface normal variations caused by deformation due to melt motion strongly affect both the absorbed power flux and the local escaping thermionic current. As a consequence, they also have a strong impact on the surface topology and should be considered in modelling. Their implementation led to material build-up along a thin ridge concentrated on one side of the sample, thus providing an interpretation for the irregular structures observed in the experiment. More elaborate heat flux loading schemes and thermionic emission specifications would need to be developed for MEMOS 3D to be able reproduce finer details of the final erosion profile of a sloped sample.

Acknowledgements

This work has been carried out within the framework of the EUROfusion Consortium and has received funding from the Euratom research and training programme 2014-2018 under grant agreement No 633053. Work performed under EUROfusion WP MST1. The views and opinions expressed herein do not necessarily reflect those of the ITER Organization or of the European Commission. SR and PT would also like to acknowledge the financial support of the Swedish Research Council.

[1] R. A. Pitts, S. Carpentier, F. Escourbiac *et al.*, *J. Nucl. Mater.* **438** (2013) S48
[2] R. A. Pitts, S. Bardin, B. Bazylev B *et al.*, *Nucl. Mat. Energy* **12** (2017) 60
[3] J. W. Coenen, V. Philipps, S. Brezinsek *et al.*, *Nucl. Fusion* **51** (2011) 083008
[4] J. W. Coenen, G. Arnoux, B. Bazylev *et al.*, *Nucl. Fusion* **55** (2015) 023010
[5] K. Krieger, M. Balden, J. W. Coenen *et al.*, *Nucl. Fusion* **58** (2018) 026024
[6] J. W. Coenen, G. F. Matthews, K. Krieger *et al. Phys. Scr.* **T170** (2017) 014013
[7] K. Krieger, B. Sieglin, M. Balden *et al. Phys. Scr.* **T170** (2017) 014030
[8] B. Bazylev, G. Janeschitz, I. Landman *et al.*, *J. Nucl. Mater.* **390-391** (2009) 810
[9] B. Bazylev and H. Wuerz, *J. Nucl. Mater.* **307-311** (2002) 69
[10] E. Thorén, B. Bazylev, S. Ratynskaia *et al.*, *Phys. Scr.* **T170** (2017) 014006
[11] M. Komm, S. Ratynskaia, P. Tolias *et al.*, *Plasma Phys. Control. Fusion* **59** (2017) 094002
[12] C. B. Vreugdenhil, *Numerical methods for shallow water flow*, Springer Science, Dordrecht, 1994

[13] P. Tolias, *Nucl. Mater. Energy* **13** (2017) 42
[14] J. A. Shercliff, *J. Fluid. Mech.* **91** (1979) 231
[15] L. Abadlia L, F. Gasser, K. Khalouk *et al.*, *Rev. Sci. Instrum.* **85** (2014) 095121
[16] M. Komm, P. Tolias, S. Ratynskaia *et al.*, *Phys. Scr.* **T170** (2017) 014069
[17] M. Komm, S. Ratynskaia, P. Tolias *et al.*, *EUROfusion Joint SOL and PSI Modelling Activities meeting*, Marseille, April 2018
[18] E. Thorén, P. Tolias, S. Ratynskaia *et al. Nucl. Fusion* (2018) in press https://doi.org/10.1088/1741-4326/aad247
[19] R. H. Cohen and D. D. Ryutov *Contrib. Plasma Phys.* **40** 2000 456
[20] J. P. Gunn, S. Carpentier-Chouchana, F. Escourbiac *et al.*, *Nucl. Fusion* **57** (2017) 046025
[21] H. Meyer *et al.*, *Nucl. Fusion* **57** (2017) 102014